INSTRUMENTATION FOR HIGH-ENERGY PHYSICS

S. Stapnes

University of Oslo, Norway

Abstract

The first part of this summary contains a description of passage of particles through matter. The basic physics processes for charged particles, photons, neutrons and neutrinos are:

– mostly electromagnetic (Bethe-Bloch, Bremsstrahlung, Photo-electric effect, Compton scattering and Pair production) for charged particles and photons,

– additional strong interactions for hadrons,

– neutrinos interacting weakly with matter.

Concepts like Radiation Length, Electromagnetic Showers, Nuclear Interaction/Absorption length and Showers are covered. Important processes like Multiple Scattering, Cherenkov radiation, Transition radiation, dE/dx for particle identification are described next. This is followed by a short discussion of momentum measurement in magnetic fields. The last part of the summary covers particle detection by means of ionization detectors, scintillation detectors and semiconductor detectors. Signal processing is briefly discussed at the end.

1. INTRODUCTION

Experimental Particle Physics is based on many advanced instruments and methods. The main instruments are accelerators with key parameters as luminosity, energy and particle type. Next follow the detectors with key parameters efficiency, speed, granularity and resolution. The online data-processing, the trigger/DAQ, all have to operate with high efficiency, large compression factors and through-put, optimized for various physics channels. The offline analysis aims to extract and understand signal and background and ultimately improve our physics models and understanding.

In this chain we should keep in mind that the primary factors for a successful physics measurement are the accelerator and detector/trigger systems and losses there are not recoverable. New and improved detectors are therefore extremely important for our field.

2. ENERGY LOSS IN MATTER

We will first concentrate on electromagnetic forces since a combination of their strength and range make them the primary responsible for energy loss in matter. For neutrons, hadrons generally and neutrinos strong and weak interactions enter in addition.

2.1. Heavy charged particles

Heavy charged particles transfer energy mostly to the atomic electrons causing ionization and excitation. We will later come back to light charged particles, in particular electrons/positrons. Usually the Bethe–Bloch formula is used to describe the energy loss of heavy charged particles. Most of the features of the formula can be understood from a very simple model:

[1] Consider the energy transfer to a single electron from a heavy charged particle passing at a distance b,

[2] Let us multiply with the number of electrons passed,

[3] Let us integrate over all reasonable distances b.

The impulse transferred to the electron will be:

$$I = \int F\,dt = e \int E_\perp \frac{dx}{\nu} = \frac{2ze^2}{b\nu} \; .$$

The integral is solved by using Gauss' law over an infinite cylinder centered along the particle track. The energy transfer is therefore:

$$\Delta E(b) = \frac{I^2}{2m_e} \; .$$

The energy transfer to a volume dV, where the electron density is N_e, can now be calculated:

$$-dE(b) = \Delta E(b)\,N_e\,dV_e \; ; \quad dV = 2\pi b\,db\,dx \; .$$

The energy loss per unit length is hence given by:

$$-\frac{dE}{dx} = \frac{4\pi z^2 e^4}{m_e \nu^2}\,N_e\,\ln\frac{b_{\text{max}}}{b_{\text{min}}} \; .$$

b_{min} is not zero but can be determined by the maximum energy transferred in a head-on collision. b_{max} is given by that we require the perturbation to be short compared to the period ($1/\nu$) of the electron.

Finally we end up with the following:

$$-\frac{dE}{dx} = \frac{4\pi z^2 e^4}{m_e \nu^2}\,N_e\,\ln\frac{\gamma^2 m_e \nu^3}{ze^2 \overline{\nu}} \; ,$$

which should be compared to the Bethe–Bloch formula below (note: dx in Bethe–Bloch includes density (g cm^{-2})):

$$\left\langle \frac{dE}{dx} \right\rangle = -4\pi N_A\,r_e^2\,m_e\,c^2\,z^2\,\frac{Z}{A}\,\frac{1}{\beta^2}\left[\frac{1}{2}\ln\frac{2m_e c^2 \gamma^2 \beta^2}{I^2}\,T_{\text{max}} - \beta^2 - \frac{\delta}{2} \right] \; .$$

Bethe–Bloch parameterize over momentum transfers using I (the ionization potential) and T_{max} (the maximum transferred in a single collision). The correction δ describes the effect that the electric field of the particle tends to polarize the atoms along its path, hence protecting electrons far away (this leads to a reduction/plateau at high energies). The curve has minimum at $\beta = 0.96$ ($\gamma\beta = 3.5$) and increases slightly for higher energies; for most practical purposes one can say the curve depends only on β (in a given material). Below the Minimum Ionizing point the curve follows $\beta^{-5/3}$. At low energies other models are useful (as shown in Fig. 1 below).

The radiative losses seen in Fig. 1 at high energy will be discussed later (in connection with electrons where they are much more significant at lower energies).

Since particles with different masses have different momentum for the same β, the dE/dx curves for proton, pions, kaons, etc are shifted with respect to each other along the x-axis when dE/dx is plotted as function of momentum. This can be used for particle identification at relatively low energies in tracking chambers (see Section 3.3).

While Bethe–Bloch describes the average energy deposition, the probability distribution in thin absorbers is described by a Landau distribution. Other functions are often used: Vavilov for slightly thicker absorbers, Bischel (Refs. [1,4]).

In general these are skewed distributions (Fig. 2) tending towards a Gaussian when the energy loss becomes large (in thick absorbers). One can use the ratio between energy loss in the absorber under study and T_{max} from Bethe–Bloch to characterize the absorber thickness.
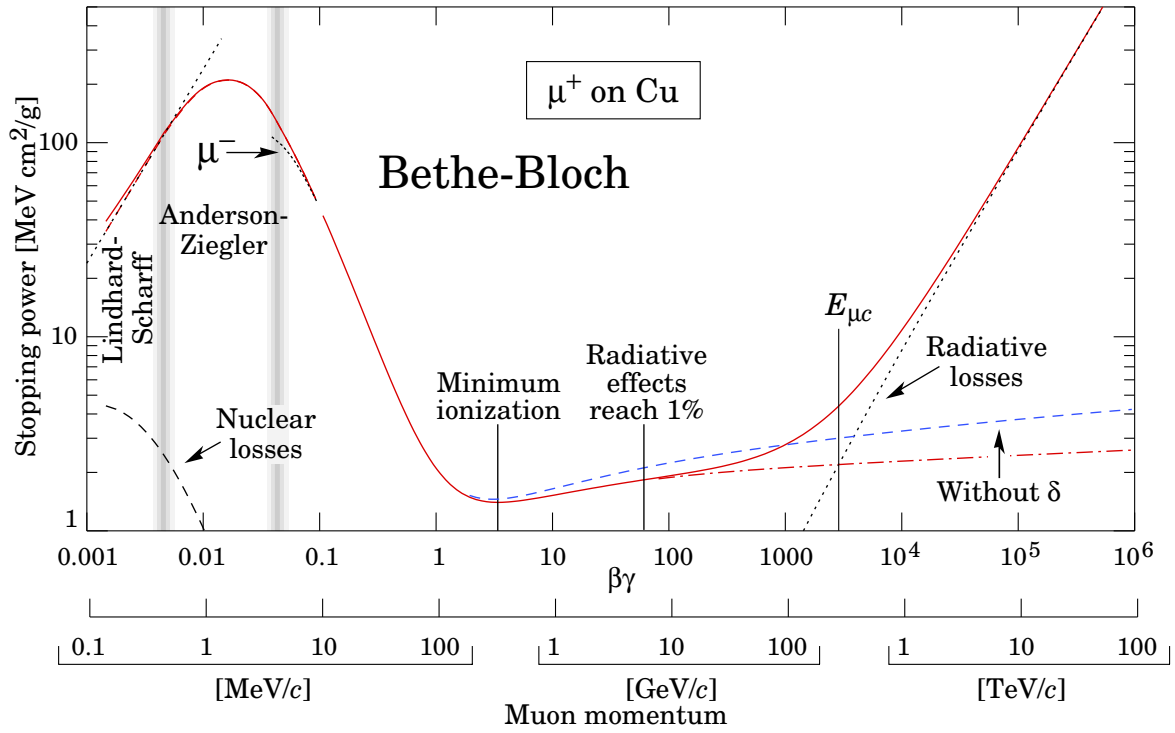
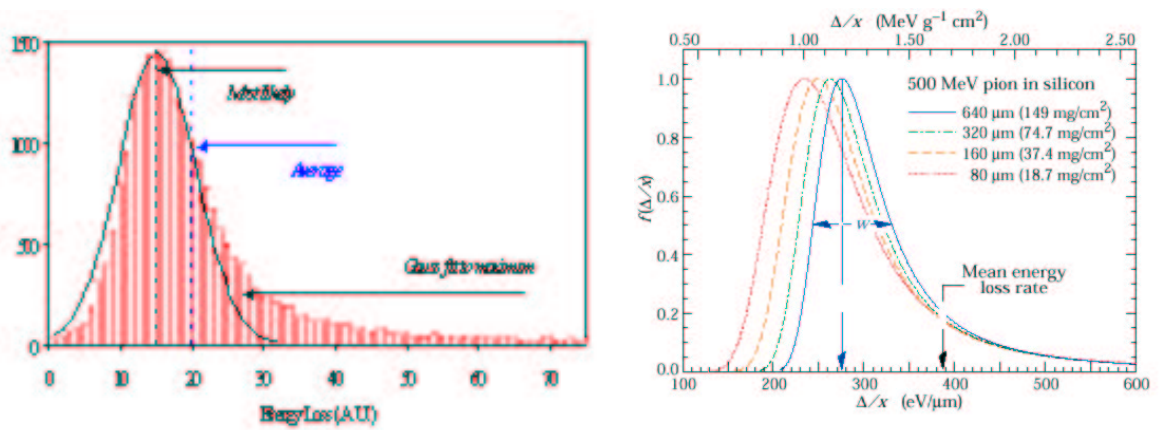Fig. 1: Radiation loss of muons in matter. From Ref. [4].

Fig. 2: Distribution of energy-loss in absorbers of varying thickness. From Refs. [1,4].

2.2. Light charged particles, electrons and positrons

For electrons/positrons the Bethe–Bloch formula has to be modified to take into account that incoming particle has same mass as the atomic electrons. In addition a significant amount of energy is carried away by bremsstrahlung photons. The cross-section for this process goes as $1/m^2$ and is therefore very significant for electrons/positrons even though it also plays a role at higher energy for muons, as seen in Fig. 1.
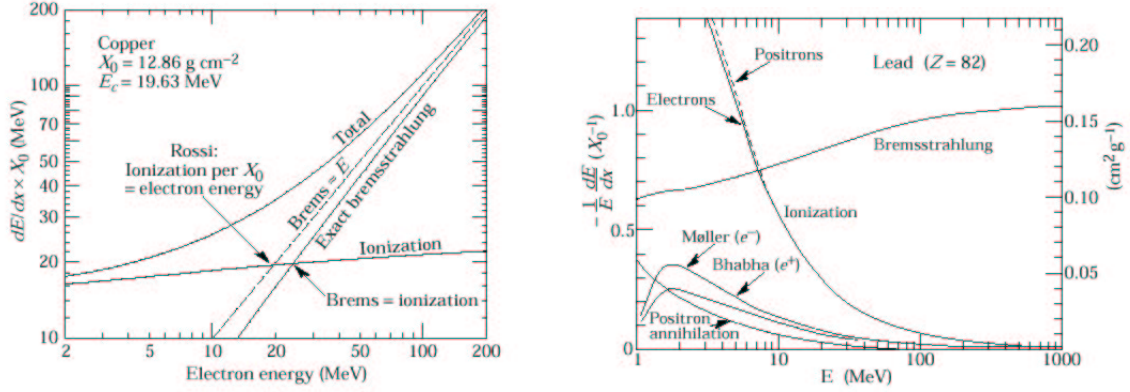

Fig. 3: Energy loss of electons in copper and lead as function of electron energy. The critical energy is defined as the point where the ionization loss is equal the bremsstrahlung loss.

The differential cross section for bremsstrahlung (ν is the photon frequency) in the electric field of a nucleus with atomic number Z is given by (approximately):

$$d\sigma \propto Z^2 \frac{d\nu}{\nu}.$$

The bremsstrahlung loss is therefore:

$$-\left(\frac{dE}{dx}\right) = N \int_0^{\nu_0 = E_0/h} h\,\nu\,\frac{d\sigma}{d\nu}\,d\nu = N\,E_0\,\Phi(Z^2),$$

where the linear dependence on energy is apparent. The Φ function depends on the material (mostly); for example on the square of the atomic number as shown. N is the atom density of the material. Bremsstrahlung in the field of the atomic electrons must be added (giving $Z^2 + Z$). The equation above can be rewritten as:

$$-\left(\frac{dE}{E}\right) = N\,\Phi dx, \quad \text{giving} \quad E = E_0 \exp\left(\frac{-x}{1/N\Phi}\right)$$

Radiation length, usually called X_0, is defined as the thickness of material where an electron will reduce its energy by a factor $1/e$ by bremsstrahlung losses. This corresponds to $1/N\Phi$ as shown above. Radiation length is often parametrised in terms of well-known material properties. A formula which is good to 2.5% (except for helium) is:

$$X_0 = \frac{716.4\,\text{g cm}^{-2}\,A}{Z(Z+1)\ln(287/\sqrt{Z})}.$$

Multiplying with the density for the various materials we find: air $\cong$ 300 m, plastic scintillators $\cong$ 40 cm, Si $\cong$ 9 cm, Pb = 0.56 cm, Fe = 1.76 cm.

2.3. Photons

Photons are important for many reasons. They appear in detector systems as primary photons, they are created in bremsstrahlung and de-excitations, and they are used for medical applications, both imaging and radiation treatment.

They react in matter by transferring all (or most) of their energy to electrons, which then lose energy as described above. A beam of photons therefore does not lose energy gradually; it is attenuated in intensity (only partly true due to Compton scattering). The most significant processes are shown in Fig. 4 below (from Ref. [4]).
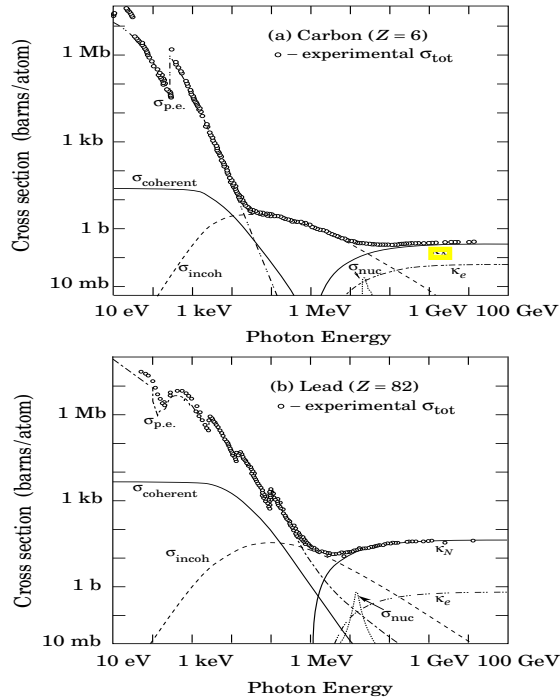

Fig. 4: Three processes dominate the photon energy loss: 1) Photoelectric effect (goes roughly as Z^5); absorption of a photon by an atom ejecting an electron. The cross-section shows the typical shell structures in an atom. 2) Compton scattering (Z); scattering of an electron against a free electron (Klein Nishinas formula). This process has well defined kinematic constraints (giving the so called Compton Edge for the max energy transfer to the electron) and for energies above a few MeV 90% of the energy is transferred. 3) Pair-production ($Z^2 + Z$); essentially the bremsstrahlung process again with the same machinery as used earlier, with a threshold at $2m_e = 1.022$ MeV. As with bremsstrahlung for electrons this process dominates at high energies.

Considering only the dominating effect at high energy, the pair production cross-section, we can calculate the mean free path of a photon based on this process alone, and find:

$$\lambda^{photon} = \frac{\int x \exp(-N\sigma_{pair}x)dx}{\int \exp(-N\sigma_{pair}x)dx} \cong \frac{9}{7} X_0 \, .$$

This shows that around one radiation length is a typical thickness for both bremsstrahlung losses (by $1/e$) and pair-production processes.

2.4. Electromagnetic calorimeters

By considering only bremsstrahlung and pair production, dominating at energies above a few tens of MeV, with one splitting per radiation length (either bremsstrahlung or pair production), we can extract a good model for EM showers.

In such a model the number of tracks increase with number of radiation lengths t as $N(t) = 2^t$. The energy carried by each particle decreases as $E(t) = E_0/2^t$. This process stops as the energy reduces to the critical energy E_C. After this point the dominating processes are ionization losses, Compton scattering and photon absorption. From this the following simple relations can be extracted: the maximum number of tracks, i.e the shower maximum, is reached at $t_{max} = \ln(E_0/E_C)/\ln 2$. The total number of
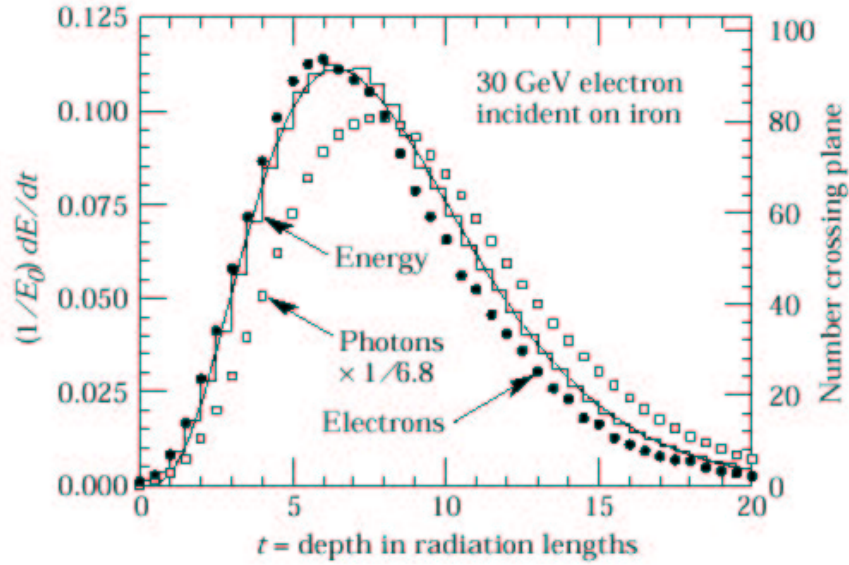
Fig. 5: Energy loss profile, measures and simulated, of electrons and photons (from Ref. [4])

tracks T is $2^{(t_{max}+1)} - 1 \approx 2E_0/E_C$. The total track length is given by $E_0 X_0/E_C$. The intrinsic relative resolution of a calorimeter is therefore improving with energy:

$$\frac{\sigma(E)}{E} \propto \frac{\sigma(T)}{T} \propto \frac{1}{\sqrt{T}} \propto \frac{1}{\sqrt{E}}$$

Furthermore, the depth needed to contain the shower increases only logarithmically.

In reality calorimeter resolutions are parameterized also with additional terms to take into account effects of in-homogeneities, cell inter-calibrations, non-linearity, and electronics noise and pile-up (a constant term and an $1/E$ term).

The typically EM shower is 95% contained in a transverse cylinder with radius $2R_n = 21$ MeV X_0/E_C: which should be compared to full longitudinal containment which requires around $25 X_0$.

The best performance of EM calorimeters is traditionally achieved with homogeneous crystal calorimeters, typical examples are BGO, CsI, NaI and PWO. The radiations length of these materials are 1–2 cm. Drawbacks are costs, radiation effects and temperature dependence. Sampling calorimeters are often used in large calorimeter systems, where a fraction of the total energy is sampled and the functions of particle absorption (often Pb) and shower sampling (scintillators, ionization detectors, silicon) are separated.

2.5. Neutrons, hadronic absorption/interaction length and hadronic showers

Neutrons have no charge and interact with matter through the strong nuclear force. They transfer energy to charged particles by elastic scattering against protons (below 1 GeV), and are absorbed/captured in materials below 20 MeV (see Fig. 6). Above 1 GeV hadronic cascades are created.

We can define hadronic absorption and interaction lengths by the mean free path of hadrons, using the inelastic or total cross-section for high energy hadrons (above GeV the cross-sections vary little for different hadrons or energy). This is in analogy to the relation between the radiation length and the mean free part of a high energy photon. In the table below (extracted from Ref. [4]) radiation lengths and interactions lengths for various materials are listed.
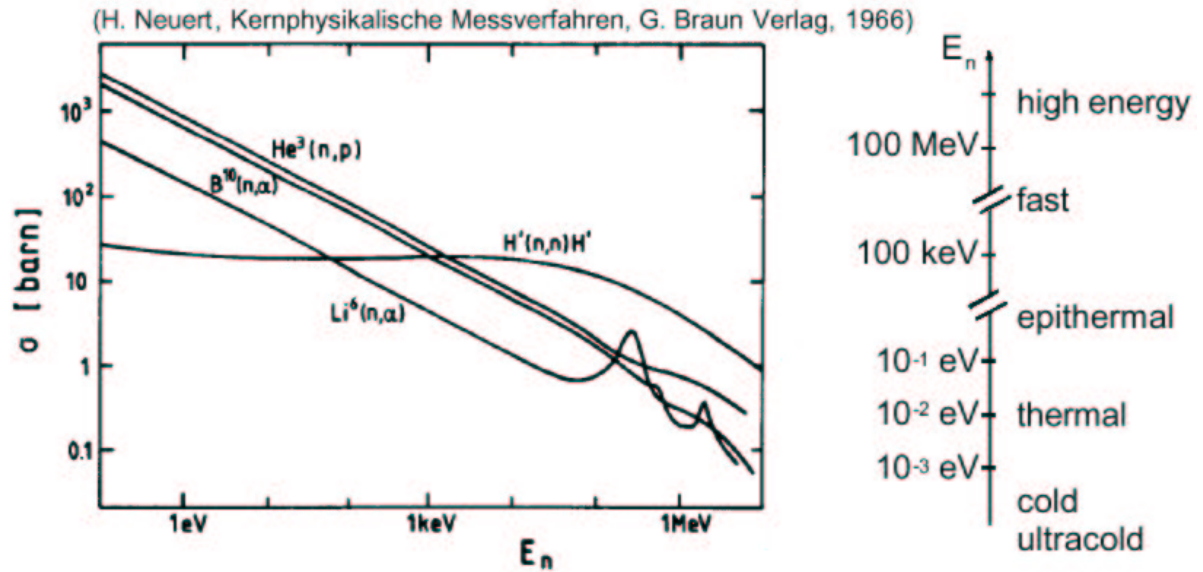
Fig. 6: Cross-sections for various neutron processes. The reference is shown in figure.

Table 1: Radiation and interaction lengths for various materials

Material	Z	A	ρ (g/cm^3)	X_0 (g/cm^2)	Λ (g/cm^2)
Hydrogen (gas)	1	1.01	0.0899 (g/l)	6.3	50.8
Beryllium	4	9.01	1.848	65.2	75.2
Silicon	14	28.09	2.33	22	106.4
Iron	26	55.85	7.87	13.9	131.9
Lead	82	207.19	11.35	6.4	194.0

Hadronic calorimeters usually have thickness around 7–8 hadronic interaction lengths (Fig. 7). Their resolution is worse than for electromagnetic calorimeters for a variety of reasons: there are significant fluctuations between the electromagnetic ($\pi_0 \rightarrow 2\gamma$) and hadronic parts (mostly charged pions) of the showers which has to be dealt with, a significant amount of the hadronic energy is lost in breakup of nuclear binding, muons and neutrinos are created in the shower escaping partly or fully, etc. The key element for good hadronic calorimeters is therefore to understand or minimize the differences between neutral pion (i.e. photons) and charge pion response and several methods are used, compensation, use of tracking information, use of longitudinal sampling information. Good coverage, uniform response and adequate granularity in depth and in angular coverage are other important parameters for hadronic calorimetry.

2.6. Neutrinos

Neutrinos react very weakly with matter. For example, the cross-section for $\nu_e + n \rightarrow e^- + p$ above a few MeV is around 10^{-43} cm^{-2} which means that in 1 m iron the reaction probability is 10^{-17}. Neutrino experiments are therefore very massive and require high fluxes.
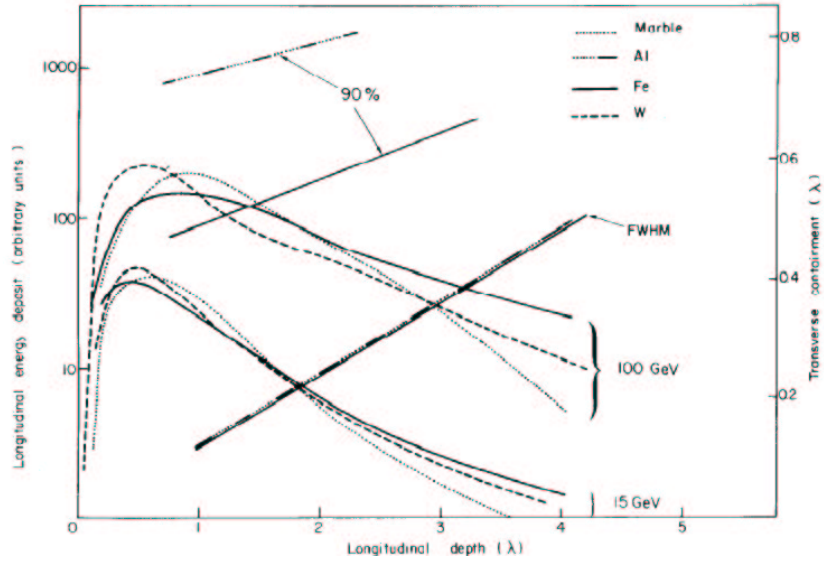
Fig. 7: Hadronic shower profiles for hadrons in various materials. The reference is shown in figure.

In collider experiments fully hermetic detectors allow to detect neutrinos indirectly. The recipe is:

- Sum up all visible energy and momentum in the detector.
- Attribute missing energy and momentum to escaping neutrino.

The most typical example was the UA1 and UA2 discoveries of $W \to e\nu$ where this method was used.

3. PARTICLE IDENTIFICATION, MAGNETIC FIELDS AND COMBINED DETECTOR CONFIGURATIONS

Section 2 summarises how most "stable" particles react with matter. We are interested in all important parameters of the particles produced in an experiment: momentum, energy, velocity, charge, lifetime and particle type.

In Section 3 we will look at some specific measurements where "special effects" or optimized detector configurations are used. Cherenkov and Transitions radiation are important in detector systems since these effects can be used for particle ID and tracking, even though the energy loss is small. This naturally leads to particle identification with various methods: dE/dx, Cherenkov, TRT, EM/HAD, p/E. Secondary vertices/lifetime measurements and combinatorial analysis provide information about c, b-quark systems, τ's, converted photons, neutrinos, etc. Finally we will look at magnetic systems and multiple scattering.

3.1. Cherenkov radiation

A particle with velocity $\beta = v/c$ in a medium with refractive index n may emit light along a conical wave front if the speed is greater than speed of light in this medium: c/n. The angle of emission (see Fig. 8) is given by:

$$\cos \vartheta = \frac{c/nt}{\beta ct} = \frac{1}{\beta n}$$

and the number of photons by:

$$N[\lambda_1 \to \lambda_2] = 4.6 \cdot 10^6 \left[\frac{1}{\lambda_2(A)} - \frac{1}{\lambda_1(A)} \right] L(\text{cm}) \sin^2 \vartheta .$$
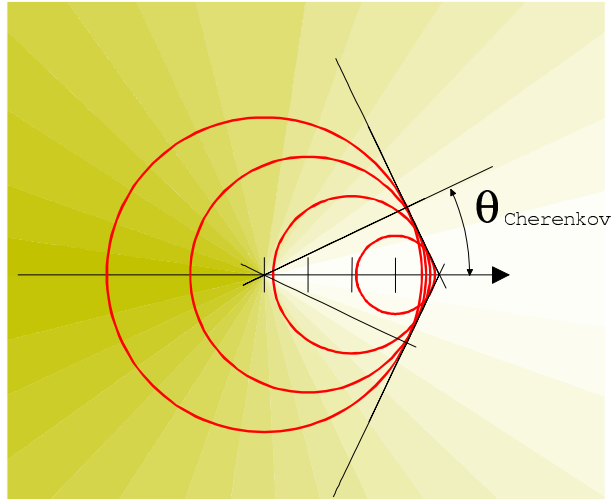
204

Fig. 8: Cherenkov radiation

In many cases a Cherenkov threshold detector is used to identify particle of a special type, typically electrons in a beamline. The Cherenkov angle will vary from slightly above 1 degree in case of air to above 45 degrees for quartz. Generally, by measuring this angle the speed of the particle can be measured. When combined with momentum information this provides a powerful particle identification tool. The number of photons is small and furthermore one has to take into account detection efficiency of the photons. The goal is to reconstruct a ring in order to provide a measurement of the emission angle and hence the β of the particle.

An example of the DELPHI Ring Image Cherenkov system is shown in Fig. 9. This is a very sophisticated detector which combines a liquid (C_6F_{14}) and a gas radiator (C_5F_{12}/C_4F_{10}), together with a photon detector (TMAE).
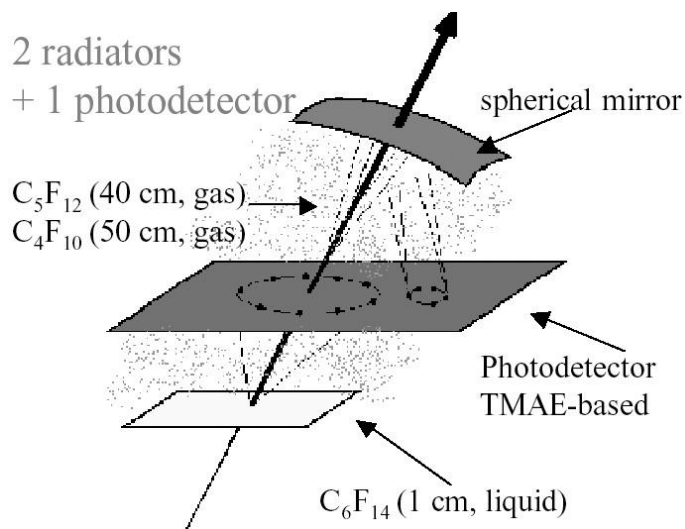

Fig. 9: Principle of Ring Imaging Cherenkov Detector (DELPHI) from Ref. [2], showing the geometrical setup that allows measurement of the Cherenkov angle. The photon detector must have a high efficiency and be built out of light materials, and hence it is a significant challenge in itself.
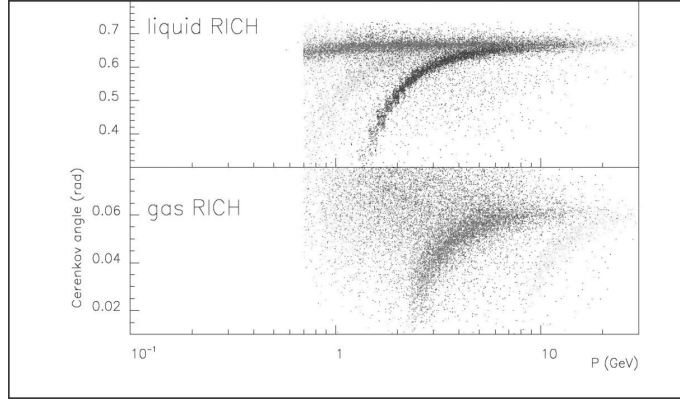
Fig. 10: Cherenkov angle in radians as function of momentum (GeV) for the DELPHI RICH. The data is in blue p from Λ, in green K from ΦD^*, in red p from K_0.

3.2. Transition radiation

Electromagnetic radiation is emitted when a charged particle transverses a medium with discontinuous refractive index, as the boundary between vacuum and a dielectric layer. More details can be found in Ref. [5].

The number of photons are small so many transitions are needed. Hence a stack of radiation layers is interleaved by active detector parts. The emission is proportional to γ so only high energy electrons/positrons will emit transition radiation. The energy per boundary is given by

$$W = \frac{1}{3}\alpha\hbar\omega_p\gamma$$

and the plasma frequency for a plastic radiator:

$$\hbar\omega_p = \hbar\sqrt{\frac{N_e e^2}{\varepsilon_0 m_e}} \approx 20\text{eV} .\tag{1}$$

The keV range photons ($\frac{1}{4}\hbar\omega_p\gamma$, see Fig. 11) are emitted at a small angle: $\vartheta \propto 1/\gamma$. The number of photons can be estimated as: The number of photons can be estimated as: $W/\hbar\omega_p\gamma \propto \alpha$.
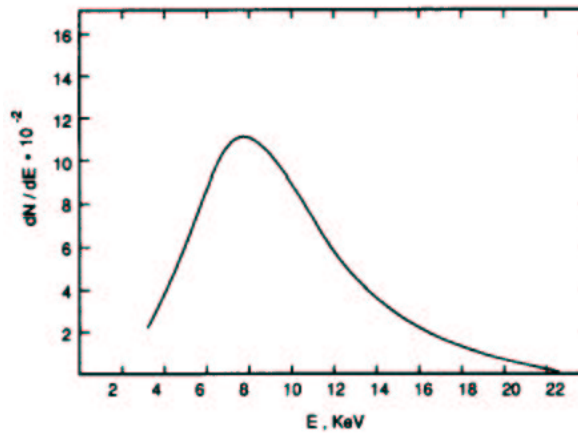

Fig. 11: Simulated spectrum from Transition Radiation in a stack of CH_2 foils (from Ref. [2]).

The radiation stack has to be transparent to these photons (low Z), and hence hydrocarbon foams and fibre materials are used. The detectors have to be sensitive to the photons (high Z, for example Xe (Z=54)) and at the same time be able to measure dE/dx of the "normal" particles which have significantly lower energy deposition.

3.3. Particle identification with dE/dx

Going back to the Bethe-Bloch plot in Fig. 1 of Section 2.1 one can see that particles with different masses will in a certain momentum range have different average energy-loss. This is exploited to identify particles. dE/dx measurements are used to identify particles at relatively low momentum. The figure below shows data from the PEP4 TPC with 185 samples (many samples important to handle statistical fluctuations). It can be seen that this method provides efficient particle identification.
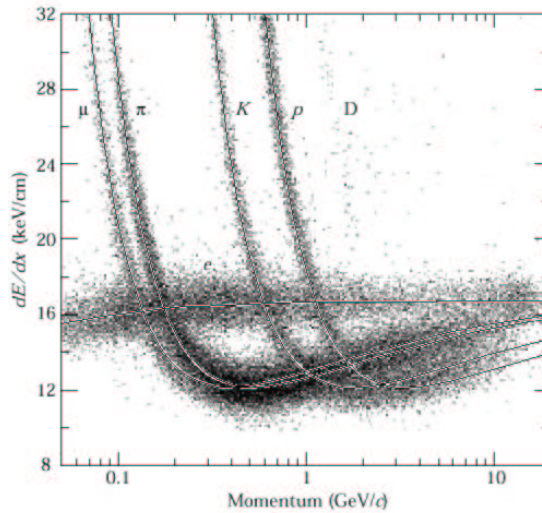

Fig. 12: dE/dx measured in the PEP4 TPC (Ref. [4]).

3.4. Momentum measurements in a magnetic field and multiple scattering

Consider a particle with charge q and transverse momentum p_T moving in a uniform magnetic field B going into the transverse plane, over a length L. The relations between the transverse momentum p_T and the radius of curvature ρ is given by $p_\mathrm{T} = qB\rho$. Expressing momentum in GeV/c and the magnetic field in Tesla, and considering q equal the elementary charge this gives p_T (GeV/c) = 0.3 $B\rho$ (T m).
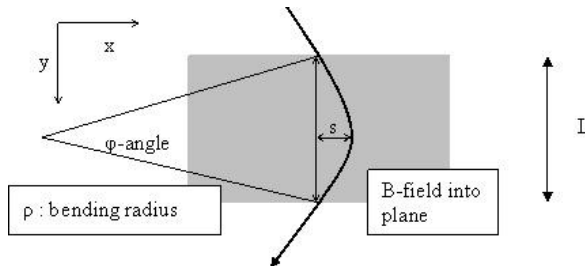

Fig. 13: Bending of a charged particle in magnetic field B

207

Measuring the momentum: Since ρ is much larger than L, as can be seen from the formula above for particles in the GeV range, we can (see Fig. 13) extract the following relations between the sagitta s and the transverse momentum p_T:

$$\frac{L}{2\rho} = \sin\frac{\vartheta}{2} \approx \frac{\vartheta}{2},$$

$$s = \rho\left(1 - \cos\frac{\vartheta}{2}\right) \approx \rho\frac{\vartheta^2}{8} \approx \frac{0.3}{8}\frac{L^2 B}{p_T}.$$

By measuring the sagitta $s = x_2 - (x_1 + x_3)/2$, where x is measured at entrance, middle, exit of the field region in Fig. 13, we can therefore measure p_T of the particle. Furthermore, the measurement precision is given by:

$$\frac{\sigma(p_T)}{p_T} = \frac{\sigma(s)}{s} = \frac{\sqrt{\frac{3}{2}}\,\sigma(x)}{s} = \frac{\sqrt{\frac{3}{2}}\,\sigma(x)\,8\,p_T}{0.3BL^2}.$$

The measurement uncertainty increases linearity with p_T. If N equidistant measurements are used the expression becomes (Ref. [6]):

$$\frac{\sigma(p_T)}{p_T} = \frac{\sigma(x)\,p_T}{0.3BL^2}\sqrt{720/(N+4)}, \qquad \text{for} \qquad N \geq 10\,.$$

Multiple scattering processes will influence the measurement. The cross-section for the scattering between an incoming particle with charge z and a target of nuclear charge Z is given by Rutherford's formula:

$$\frac{d\sigma}{d\Omega} = 4\,z\,Z\,r_e^2\left(\frac{m_e c}{\beta\,p}\right)^2\frac{1}{\sin^4\vartheta/2}$$

For sufficiently thick materials the particle will undergo multiple scattering and usually a Gaussian approximation (Ref. [4]) for the scattering angle distribution is used with a width expressed in terms of radiation lengths (good to 11% or better):

$$\vartheta_0 = \frac{13.6\ \text{MeV}}{\beta\,c\,p}\,z\,\sqrt{x/X_0}\,[1 + 0.038\,\ln(x/X_0)]\,.$$

The multiple scattering over the distance L mentioned above will influence the momentum as follows:

$$\Delta p^{\text{MS}} = p\,\sin\vartheta_0 \approx 0.0136\sqrt{\frac{L}{X_0}}\,.$$

This should be compared to the change in momentum over the same distance L due to the effect of the magnetic field, see Fig. 13: $0.3\,BL$.

$$\left.\frac{\sigma(p_T)}{p_T}\right|^{\text{MS}} = \frac{\Delta p^{\text{MS}}}{0.3\,BL} = \frac{0.0136\sqrt{\frac{L}{X_0}}}{0.3\,BL} = 0.045\frac{1}{B\sqrt{L\,X_0}} \qquad \text{independent of } p\,.$$

The resulting total momentum resolution, adding the two contributions in quadrature, is shown in the figure below (from Ref. [2]).
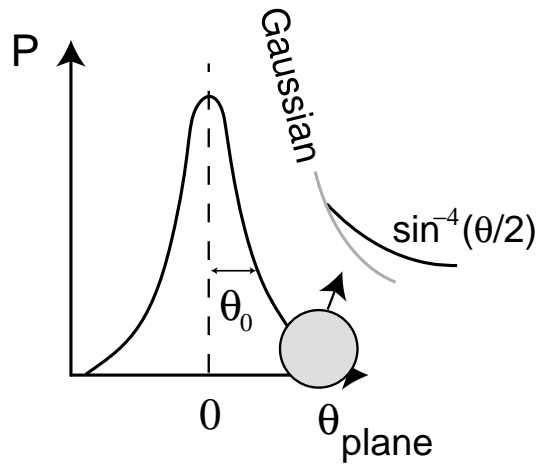
Fig. 14: Gaussian approximation of a multiple scattering distribution, indicating also that the initial Rutherford formula will increase the tails. From Ref. [2].
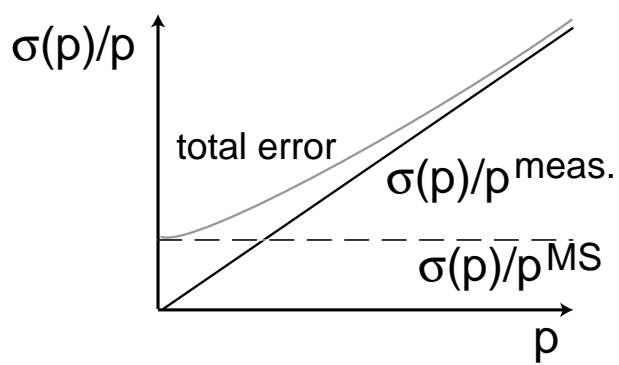

Fig. 15: The measurement uncertainty introduced a linear term in the momentum resolution while multiple scattering introduces a constant term.

3.5. Vertexing and secondary vertices

Several important measurements in particle physics depend on the ability to tag and reconstruct particles coming from secondary vertices hundreds of microns from the primary (giving track impact parameters in the tens of micron range), to identify systems containing b, c, τ, etc, i.e. generally systems with these types of decay lengths.

This is naturally done with precise vertex detectors where three features are important:

- Robust tracking close to vertex area.
- The innermost layer as close as possible to the collision point.
- Minimum material before first measurement in particular to minimise the multiple scattering (beam pipe most critical).

The vertex resolution is usually parameterized with a constant term (geometrical) and a term depending on $1/p \sin^{3/2} \vartheta$ (multiple scattering), where ϑ is the angle to the beam-axis.

3.6. Particle identification combining information from a detector system

In addition to the methods mentioned above we must keep mind that combining information from various parts of the detector provides powerful particle identification.

EM/HAD energy deposition information provides particle ID, EM response without a track indicates a photon, matching of p (momentum) and EM energy the same (electron ID), vertexing help us to tag b, c or τ, missing transverse energy indicates a neutrino, muon chamber hits indicate a muon, etc., so a number of combinatorial methods are finally used in experiments.
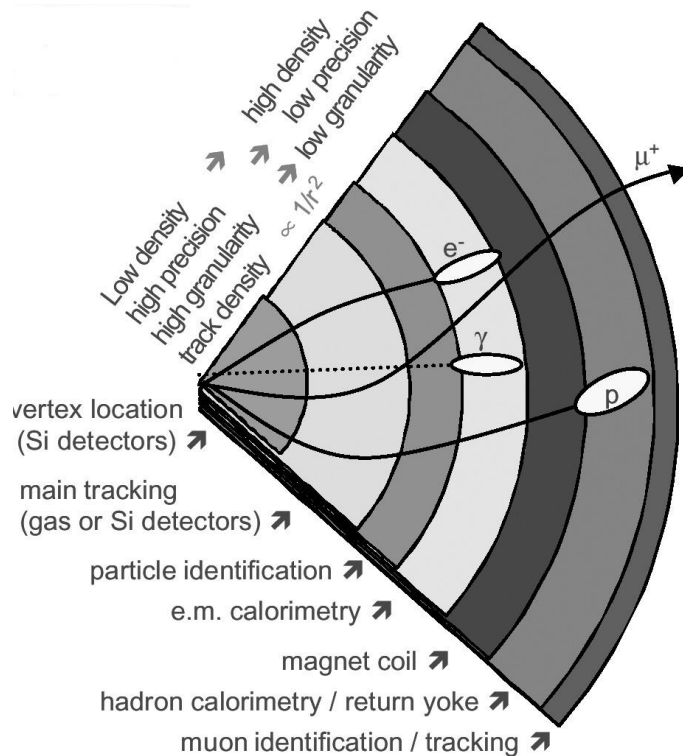

Fig. 16: A typical detector cross-section showing a tracker, particle identification, calorimeters and a muon system, together with the magnets (from Ref. [2]).

4.   ACTIVE DETECTOR ELEMENTS IN PARTICLE PHYSICS

In Sections 2 and 3 we described how most particles (i.e. all particles that live long enough to reach a detector; electrons, muons, proton, pions, kaons, neutrons, photons, neutrinos, etc) react with matter and how they are measured (p, E, v, lifetimes, charge, etc) and identified in a modern detector system. One essential step in the process was however omitted: How are reactions of the various particles with detector elements turned into electrical signals? We want position and energy deposition information, channel by channel, from our detector system.

Three detector types are usually used:

4.1 Ionization detectors

4.2 Scintillation detectors

4.3 Semi Conductor detectors

These active elements are used in either for tracking, energy measurements or photon detectors for Cherenkov or TRT. The three types have different applications, advantages and disadvantages but virtually all active elements in a complex detector system rely on these three principles.

At the end of Section 4 we will have a quick look at how electrical signals are amplified in FE electronics, and the main parameters determining the performance of readout electronics.

4.1.   Ionization detectors

A charged particle passing through matter will transfer energy to the atomic electrons causing ionization and excitation. In an ionization detector the electrons and ions created when the particle traverses or is absorbed in a medium, usually gas, are used to generate a measurable signal. The ionization potential for various gases is shown in Fig. 17. Typical numbers of primary encounters in various gases are summarised in Table 2. Since many of these encounters lead to secondary and tertiary ionizations the number of free electrons created is larger by a factor 3–4, but nevertheless the signal is very small and an amplification step is needed to increase the noise margins.
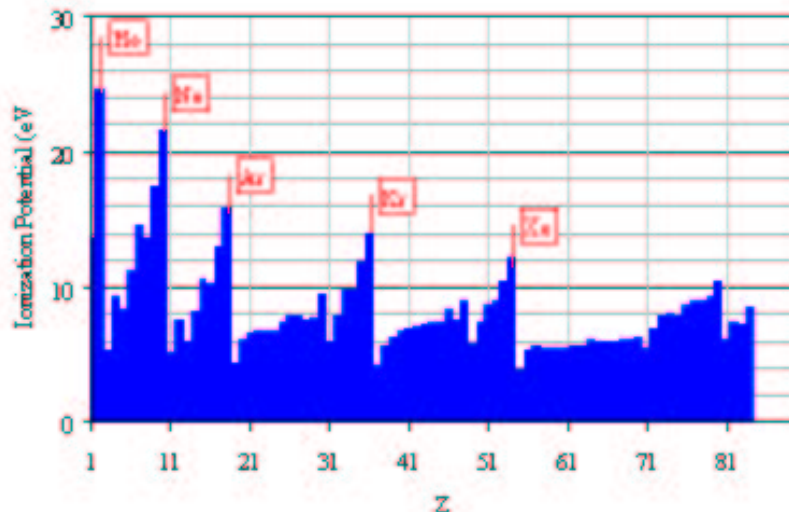

Fig. 17: Ionization potential for various elements. Primary and total number of ions/electrons created per cm in several gases (at SPT) used in proportional counters.

In the following section the amplification processes and drift in an electrical field are briefly discussed, as they provide the basis for the operation of a proportional chamber. Ionization detectors are generally

Table 2: Ionization potential for various elements. Primary and total number of ions/electrons created per cm in several gases (at SPT) used in proportional counters.

Gas	Primary electrons (1/cm)	Total electrons (1/cm)
He	5	16
Ne	12	42
Ar	25	103
Xe	46	340
CH_4	27	62
CO_2	35	107
C_2H_6	43	113
DME	55	160
i-C_4H_{10}	84	195

operated in proportional mode where an amplification of 10^4 to 10^6 is used. The response of a proportional chamber (Fig. 21) is shown in Fig. 18 as function of voltage. There are several distinctive regions of the response curve:

[1] <u>Recombination</u> before charge collection.

[2] <u>Ionization</u> chamber region; all primary charge is collected (no multiplication) giving a flat response.

[3] <u>Proportional</u> counter (gain up to 10^6), where the electric field is large enough to begin multiplication; secondary avalanches need to be quenched. At the end of this region limited proportionality is observed (secondary avalanches distort the field, more quenching is needed) and the same signal is detected independently of the original ionizing event.

[4] <u>Geiger Muller</u> mode, where strong photon emission propagates avalanches all over the wire.

The amplification process can be characterised as follows:

Let α^{-1} be the mean free path (also called the first Townsend coefficient) between each ionization. The increase in the number of produced electrons after a path dx, will be $dn = n\alpha dx$ where n is the number of initial electrons. By integration, $n = n_0 e^{\alpha x}$, therefore the gas amplification $M = n/n_0$ is given by:

$$M = e^{\int_{x_1}^{x} \alpha(x)dx} .$$

The amplification curve in a standard gas mixture such as Ar-CO_2 80–20% is shown in Fig. 19.

Another important aspect of the ionization chamber is the drift velocity. In a simple formulation, the drift velocity v_D in an electric field E can be written as:

$$v_D = \frac{e}{m} E \tau ,$$

where τ is the mean free time between collisions, in general a function of the electric field, m the mass and e the charge. Figure 20 below shows the drift of electrons under the action of the electric field (superimposed on the normal thermal movements of the gas molecules).

Different requirements apply to different chambers. If the chamber is to operate at high counting rates,
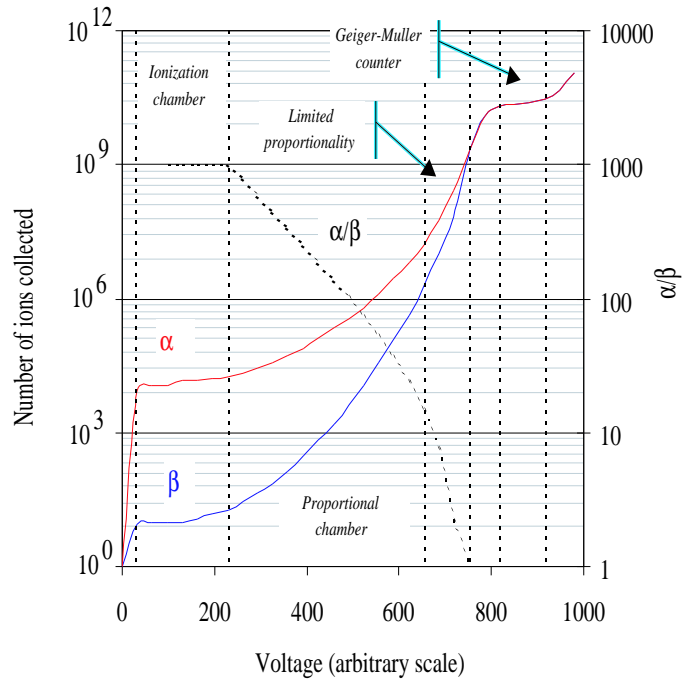
Fig. 18: Response of a proportional chamber as function of applied voltage (from Ref. [2]).

the drift velocity should be high, to avoid losses due to dead time. For better spatial resolution, drift velocities should be lower, to minimize the influence of timing errors on position resolution.

In the presence of a magnetic field, the drift velocity is generally reduced, and the drift direction is no longer along the electric field. This has to be taken into account when operating chambers close to or inside strong magnetic fields. The general operational principle of a gas detector can be understood by studying more closely a simple proportional chamber. The cross-section of such a chamber of cylindrical geometry is shown in Fig. 21, below on the right.

The cathode is a metallic cylinder of radius b. Let us consider a typical example where the anode is a gold plated tungsten wire of radius a; $a = 10^{-5}$ m and $b/a = 1000$.
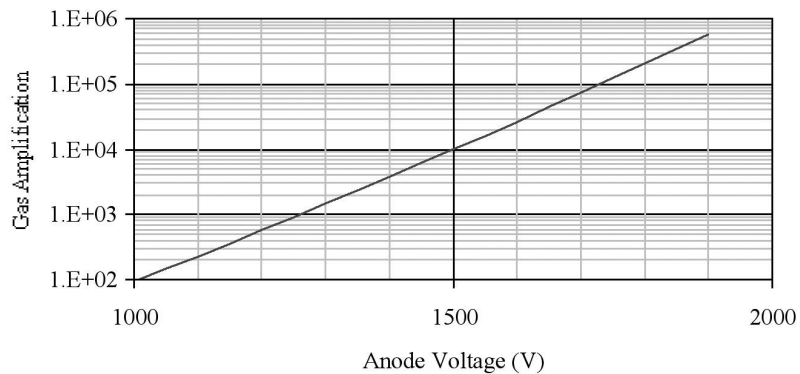

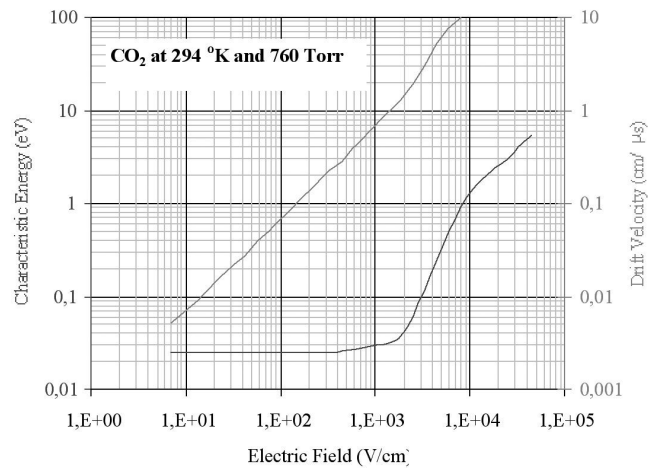Fig. 19: Gas amplification as function of voltage in Ar-CO_2 [80%–20%].

Fig. 20: Drift velocity, upper curve, as function of electric field for electrons. The drift velocity of the positive ions under the action of the electric field is linear with the reduced electric field (E/pressure) up to very high fields and several orders of magnitude lower than the electron velocity.
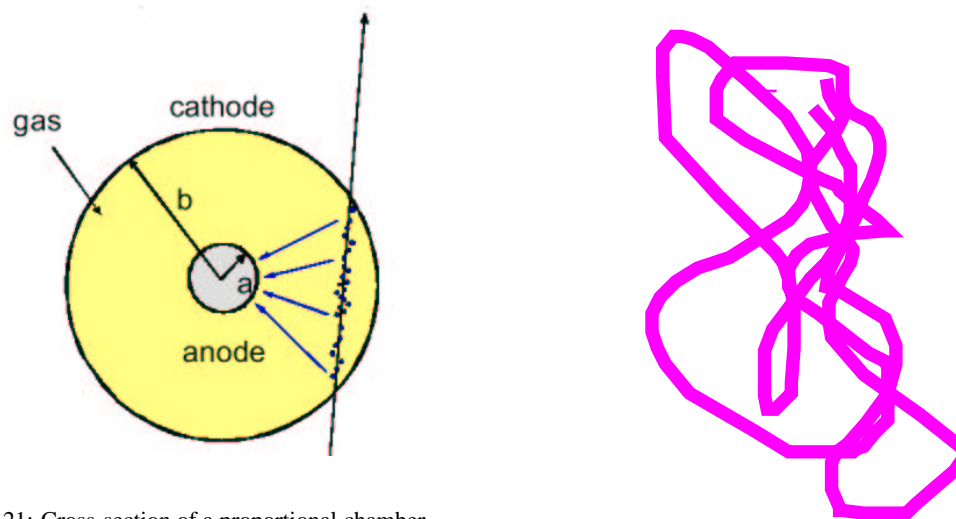

Fig. 21: Cross-section of a proportional chamber.

The electric field at a distance r from the center can be written as:

$$E(r) = \frac{1}{r} \frac{CV_0}{2\pi\varepsilon_0} \, ,$$

where C is the capacitance per unit length. Given the $1/r$ dependence, the electric field close to the anode is large and multiplication can start, therefore the development of the signal begins at a few wire radii.

The formation of signal can be understood as follows. The electrostatic energy of the configuration is: $W = \frac{1}{2} l C V_0^2$, where C is the capacitance per unit length, V_0 the over-all potential difference and l is the length of the counter. The potential energy of a charged particle at radius r is given by the charge times the potential:

$$W = -q \frac{CV_0}{2\pi\varepsilon_0} \ln \frac{r}{a} \, .$$

Considering this as an isolated system, we can set up an equation for how the voltage (signal) changes

when the particle moves in the electric field:

$$dW = l\,C\,V_0\,dV = q\frac{d\varphi(r)}{dr}\,dr\,, \qquad \text{where} \quad \varphi(r) = -\frac{C\,V_0}{2\pi\varepsilon}\ln\frac{r}{a}\,.$$

The signal is induced mainly by the positive ions created near the anode. This can be seen if we assume that all charges Q are created within a distance λ from the anode. λ is of the order of a few 10's of μm, hence $V_{electron} \cong V_{ion}/100$ which can be seen from the equations below setting in the correct values for a and b:

$$
\begin{aligned}
V_{electron} &= -\frac{Q}{lCV_0}\int_a^{a+\lambda}\frac{dV}{dr}\,dr = -\frac{Q}{2\pi\varepsilon l}\ln\frac{a+\lambda}{a}\,, \\
V_{ion} &= \frac{Q}{lCV_0}\int_{a+\lambda}^b\frac{dV}{dr}\,dr = -\frac{Q}{2\pi\varepsilon l}\ln\frac{b}{a+\lambda}\,.
\end{aligned}
$$

The time development of the signal can be computed neglecting the electron contribution and assuming all ions leaving from the wire surface:

$$V(t) = V_{ion} = \frac{Q}{lCV_0}\int_{r(0)}^{r(t)}\frac{dV}{dr}\,dr = -\frac{Q}{2\pi\varepsilon l}\ln\frac{r(t)}{a}\,.$$

The final result for $V(t)$ is shown in Fig. 22.
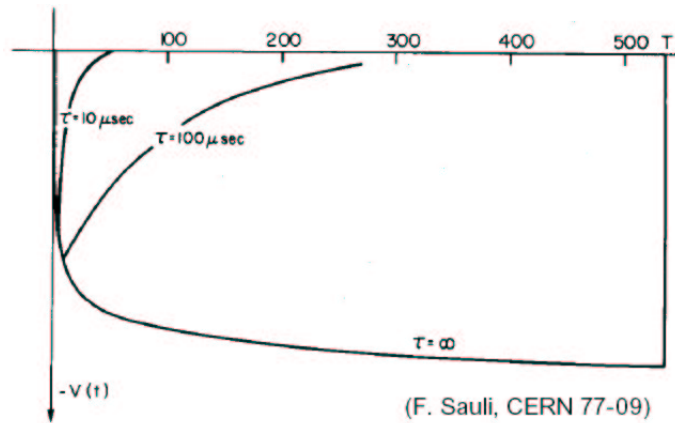

(F. Sauli, CERN 77-09)

Fig. 22: Typical signal induced in a proportional chamber. T is the total drift time of positive ions from anode to cathode. The pulse shape obtained with several differentiation time constants is also shown. Electronics differentiation is used to limit dead time. Note that one can speed up the response but at the cost of collecting only a very limited part of the signal. The initial drift-time and ultimate time response can be understood from the electron drift in the electrical field and gas-mixture used.

From the basic proportional chamber, we can now study:

– Multiwire Proportional Chambers (MWPC). An MWPC consist of a set of thin, parallel anode wires in between two cathode planes. The cathodes are at negative voltage and the wires are grounded. This creates a homogeneous electric field in most regions, with all field lines leading from the cathode to the anode wires (Figs. 23 and 24). Multiple planes with different angles of inclination for the wires allow reconstruction of trajectories in space.
Limited both by electrostatic forces and construction technology, the minimum distance in MWPC is $\sim$ 1 mm, restricting spatial resolution and rate capability. The binary readout resolution (the RMS of a square probability distribution) is given by: $pitch/\sqrt{12}$. Therefore, for a con-

ventional MWPC built with wires spaced by 1 mm, spatial resolution is limited to 300 μm. Analogue readout and charge sharing, as shown in Fig. 23 with segmented cathode plane readout, can improve this significantly when the left/right signal size provides detailed information about the hit position. In this case the resolution is limited mainly by the charge sharing mechanisms and the analogue readout resolution. These considerations apply equally well to the silicon detectors discussed in Section 4.2.
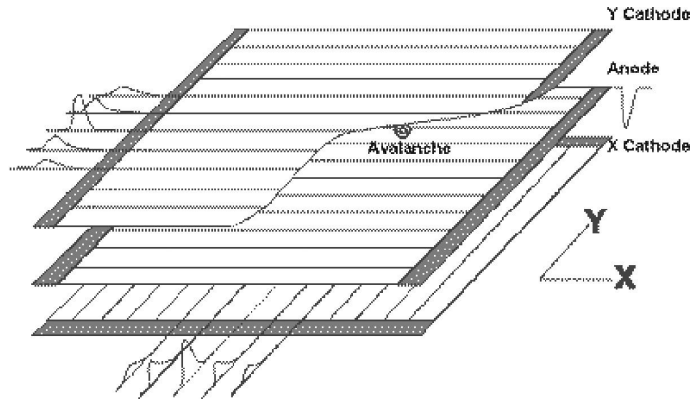
Fig. 23: The basic structure of a 2D MWPC. The avalanche occurring on the anode induces signals of opposite polarity upon the two orthogonal cathode planes. These signals are then used to produce an X and Y position of the incident particle. In general, two dimensional readout can be obtained by charge division with resistive wires, measurement of timing differences or segmented cathode planes with analogue readout as shown here. From Ref. [2].
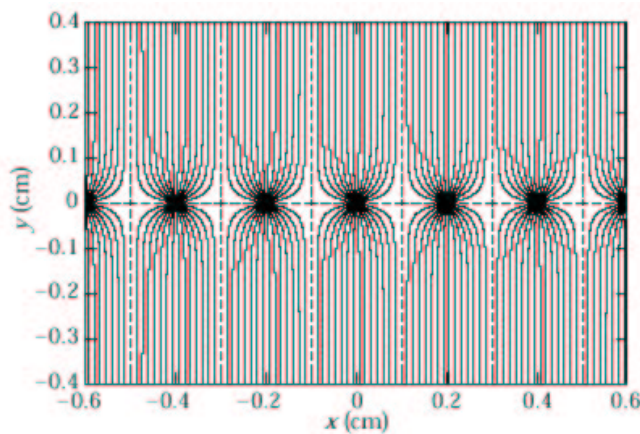

Fig. 24: Electric field equipotentials and field lines in a classic Multi-Wire Proportional Chamber (MWPC), from Ref. [2]. Typical parameters: gap between anode and cathode planes: 5 mm, wire spacing: 1–4 mm, anode wire diameter: 20 μm.

- <u>Straw Tubes.</u> The proportional chamber described above, if of small diameter, typically < 10 mm, is a perfect straw-detector unit. Among other advantages, some virtues of a straw system are the possibility of building large self-supporting structures, isolation of broken wires from its neighbors and minimum cross-talk between neighboring detector elements.

- <u>Drift Chambers</u> function the same than proportional tubes, with measurement of drift time added (time that electrons take to arrive to a sense wire, with respect to a t_0 measurement) to determine one co-ordinate. The space resolution is therefore not limited to cell size, allowing significant reduction of the number of readout channels. The distance between wires is typically 5–10 cm giving around 1–2 ms drift-time. A resolution of 50–100 μm can be achieved, limited by field uniformity and diffusion. There are however more problems with occupancy.

216

– Time Projection Chambers. The optimal chamber including all features above. They permit full 3-D track reconstruction, dE/dx and momentum measurements when used in magnetic fields (see Fig. 25). Their operation is based on:

- X and Y coordinates are given by signal readout at the end plate traditionally with conventional MWPC structures.
- Drift-time measurements provide the Z coordinate.
- Analogue readout gives dE/dx.
- Magnetic field provides p (and reduces transverse diffusion during drift).

The long drift time and the difficulty of shaping the field are drawbacks: space charge builds up, and in-homogeneities in the field can cause serious degradation of the precision. Introduction of ion-stopping grids (gates), careful tuning of the drift field (sometimes by an additional potential wire plane), and gas purity are of vital importance to the resolution achieved in these chambers.
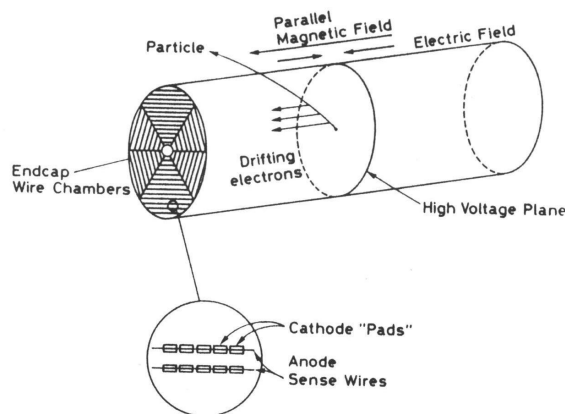

Fig. 25: A typical TPC, centered around the collision point of a collider experiment (from Ref. [1])

.

– Newer chambers and developments as Micro Strip Gas Chambers (MSGC) and detectors based on the Gas Electron Multiplier (GEM).

In recent years there have been several developments directed towards making gas detectors more suitable for high rate applications, for example as inner detector components for LHC. MSGCs have been proposed (Ref. [7]) and developed. MSGCs basically reproduce the field structure of multi-wire chambers (MWPC) with a significant scale reduction. They are made of a sequence of alternating thin metallic anode and cathode strips (typical pitch is about 100–200 μm) on an insulating support; a drift electrode on a plane above defines a region of charge collection, and application of appropriate potentials on the strip electrodes creates a proportional gas multiplication field. The intrinsic spatial resolution is about 30 μm rms using the method of centre of gravity of the amplitude pulses. The multi-track resolution is about 250 μm.

The Gas Electron Multiplier consists of a thin, metal-clad polymer foil, chemically pierced by a high density of holes (Fig. 26). By applying a potential difference between the two electrodes, electrons released by radiation in the gas on one side of the structure drift into the holes, multiply and transfer to a collection region. The multiplier can be used as a detector on its own, or as a preamplifier in a multiple structure. GEM detectors are used successfully in COMPASS (Ref. [8]). Typical spatial resolution is about 45 μm and time resolution of the order of 12 ns, though lower values can be achieved with suitable

gases. Detailed studies of gain and discharge point at high rate, and in presence of heavily ionizing tracks, have successfully demonstrated the performance of multiple GEM structures in a high rate environment.
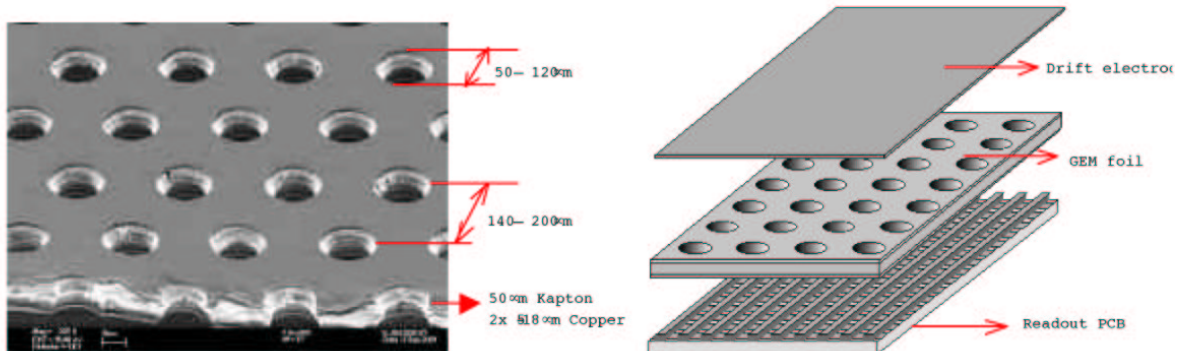

Fig. 26: On the left, SEM picture of a GEM foil. On the right, schematics of a single-GEM detector with 2D readout. The GEM foil separates a drift zone and an induction zone, leading to the readout pad or strip layer. Several GEM foils are used in cascade in some cases.

The operational advantages of these developments are based on short drift-times and use of PCB and Flex-processing techniques to create the appropriate anode/cathode configurations. A GEM readout for Time Projection Chambers is also being considered. A GEM-TPC readout end-cap may consist of several cascaded GEMs to obtain the needed amplification, and a patterned readout plane, collecting the (negative) charge.

For all gaseous detectors the choice of gas is a delicate matter. Gas is selected depending on the desired mode of operation and expected conditions of use. Most chambers run with a mixture of noble gas and a smaller fraction of a polyatomic molecule. The first allows multiplication at low electric fields; the second is chosen because it absorbs photons in a wide energy range, emitted by excited atoms in the avalanche when they return to the ground state, and suppresses secondary emission allowing high gas gains before discharge. A classical gas mixture for low rate proportional chambers is Ar-CH_4 [90%–10%]. For high-rate, fast detectors, gases with high drift velocity are used to minimize losses due to dead time and occupancy. Better spatial resolution is obtained with low drift velocity gases that minimize timing errors (CO_2 or DME). Microstructures such as MSGCs or GEMs are typical used with gases with high primary ionization statistics to reach full efficiency in thin gas gaps. Finally, radiation damage or aging of gaseous detectors is a field of continuous study. Experimentally, the progressive loss of detection efficiency or the increase of leakage current in the operating chamber will be interpreted as clear signs of aging. These effects depend on many parameters such as gas choice, gas purity and cleanliness, additives and level of impurities, flow rate, gas gain and detector geometry. Therefore, intensive R&D is needed to set the conditions needed to secure stable operation of gaseous detectors, especially in high luminosity experiments.

4.2. Scintillators

In scintillating materials the energy loss of a particle lead to an excitation, quickly followed by a de-excitation providing detectable light. Light detection/readout is therefore an important aspect of the readout of scintillators.

Scintillators are used in many physics applications. They are frequently used in Calorimetry (relatively cheap and with good energy resolution), for tracking (fibres), in Trigger Counters, for Time of Flight measurements, and in Veto Counters.

218

Inorganic scintillators are often used in calorimeters due to their high density and Z. They are relatively slow but have high light output and hence good resolution. Organic scintillators are faster but have less light output. In the following section both types are discussed further.

To convert the light into an electrical signal a chain of wavelength shifters and photon detectors is used. In this field there are constantly new developments in order to increase granularity, reduce noise and increase sensitivity.

Inorganic Crystalline Scintillators.

The most common inorganic scintillator is sodium iodide activated with a trace amount of thallium [NaI(Tl)]. NaI has a light output of typically 40000 photons per MeV energy loss. The light collection, and the quantum efficiency of the photo detector will reduce the signal further. The detector response is fairly linear.
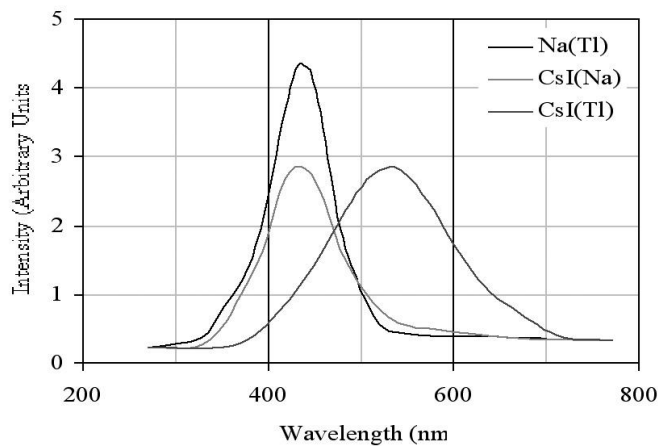
Fig. 27: The light output for NaI and CsI (Ref. [3])

Table 3: A list of the most significant parameters for commonly used scintillators (from Ref. [1]). Note that the light output is normalized to NaI.

Crystal	ρ (g/cm^3)	X_0 (cm)	$r_{\text{Molière}}$ (cm)	dE/dx (MeV/cm)	λ_I (cm)	τ_{decay} (ns)	λ_{max}	n_D	Rel. output*	Hygro
NaI(Tl)	3.67	2.59	4.5	4.8	41.4	250	410	1.85	1.00	very
BGO	7.13	1.12	2.4	9.2	22.0	300	410	2.20	0.15	no
BaF$_2$	4.89	2.05	3.4	6.6	29.9	0.7	220	1.56	0.05	slightly
						620	310		0.20	
CsI(Tl)	4.53	1.85	3.8	5.6	36.5	1000	565	1.80	0.40	some
CsI(pure)	4.53	1.85	3.8	5.6	36.5	10.36	305	1.80	0.10	some
						36, 620	~ 480		0.20	
PbWO$_4$	8.28	0.89	2.2	13.0	22.4	5–15	420–440	2.3	0.01	no
CeF$_3$	6.16	1.68	2.6	7.9	25.9	10–30	310–340	1.68	0.10	no

Organic Scintillators.

These scintillators are fast and with typical light output around half of NaI. Practical organic scintillators use solvents; typically organic solvents which release a few % of the exited molecules as photons (polystyrene in plastic for example, xylene in liquids) + large concentration of primary fluor which transfers to wavelengths where the scintillator is more transparent and changes the time constant + smaller concentration of secondary fluor for further adjustment + ...
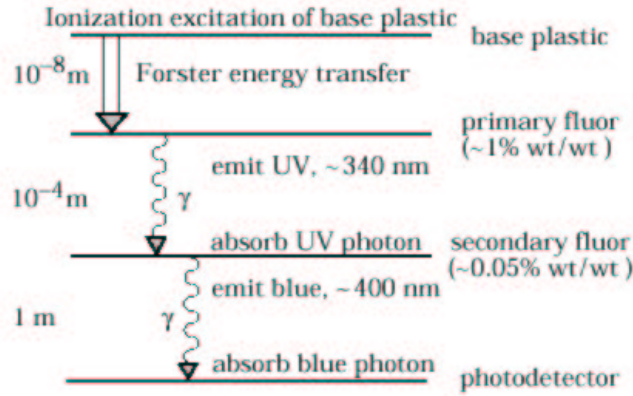

Fig. 28: Illustration of the de-excitation process, including wavelength shifting fluors, of an organic scintillator (from Ref. [4]).

Light collection and readout.

External wavelength shifters and light guides are used to aid light collection in complicated geometries. These must be insensitive to ionizing radiation and Cherenkov light.
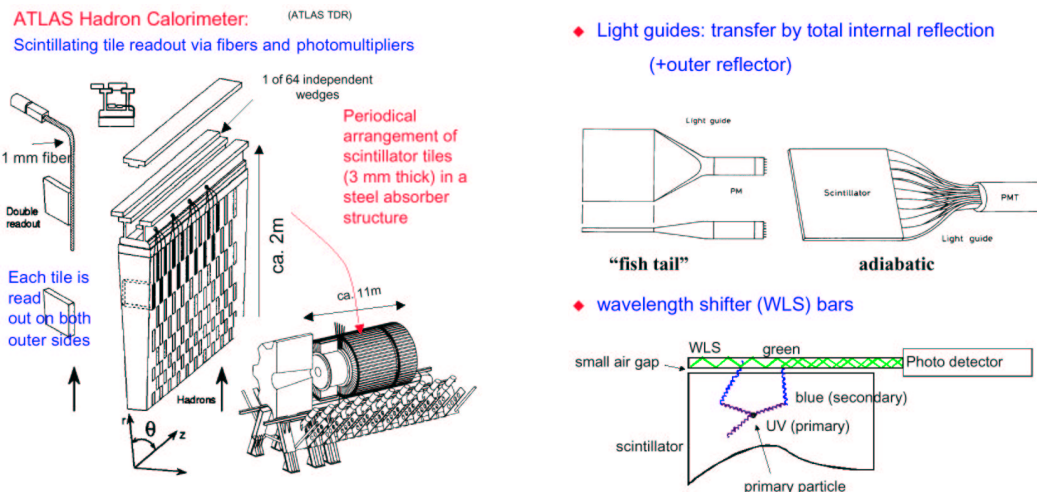
Fig. 29: In the two figures on the right a typical readout configuration is shown, with light guides, wave-length shifter and photo-detectors. The ATLAS Hadronic Calorimeter (left) is a typical example of a modern sampling calorimeter fully based on scintillators as active medium.

The most critical readout parameters for photo detectors are granularity, noise and sensitivity. Compared to the typical single channel photo multipliers, diodes and triodes, there are several new developments. As one example the multi anode PM is shown in Fig. 30. Recently, Hybrid Photo Diodes (Ref. [9]) have been developed where the dynode structure is replaced by a voltage gap and a granular silicon detector,

as shown in Fig. 30. This has the potential of removing the primary source of noise, fluctuations in the first dynode, and provides good granularity.
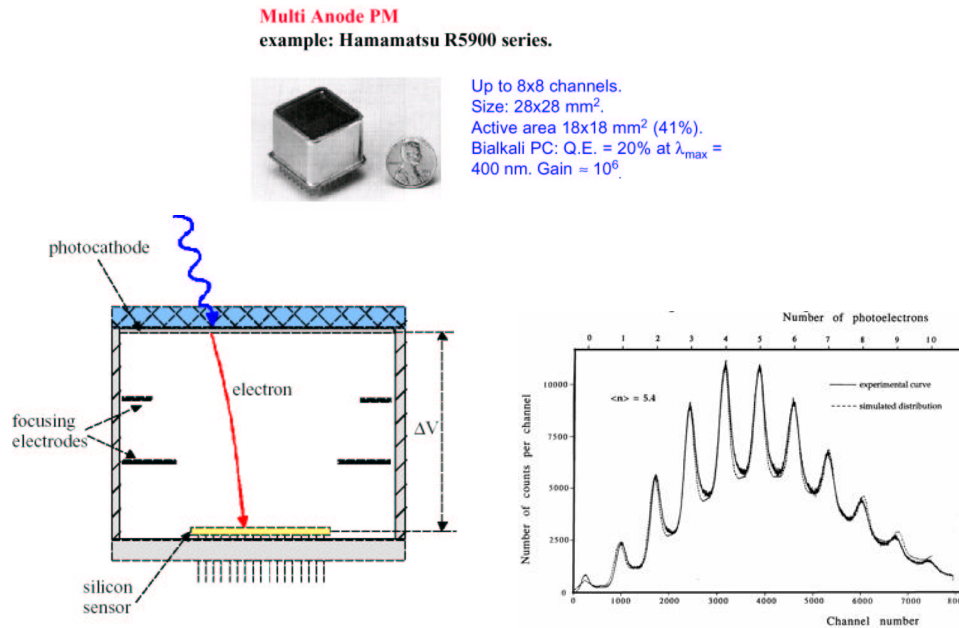

Fig. 30: Examples of new readout developments for photons aimed at increasing granularity and resolution (from Ref. [4]).

4.3. Solid-state detectors

Solid state detectors have been used for energy measurements a long time (Silicon, Germanium). It takes a few eV to create an electron–hole $(e - h)$ pair and as a result these detector materials have excellent energy resolution. Nowadays silicon detectors are mostly used for tracking and virtually every major particle physics experiment uses this technology for tracking close to the interaction point. We will concentrate on silicon in the following.

The key parameters for silicon detectors are as follows: band gap 1.1 eV while the average energy to create an $(e - h)$ pair is 3.6 eV (compared to 30–40 eV for ionization detectors), high density such that the energy loss in silicon, from Bethe-Bloch, is 108 $(e - h)/\mu$m. The mobility for electrons and holes are high, and the structures are self-supporting. More generally the successful development of modern silicon detectors rely on the progress in semi-conductor industry over the last decades. This concerns key parameters as reliability, yield, cost, feature sizes and connectivity.

Contrary to the ionization detectors there is no amplification mechanism, however S/N levels of 10–50 are common, mostly depending on the electronics noise, again depending on detector geometry (capacitive load seen by readout amplifier).

Intrinsic silicon will have electron density = hole density; $1.45 \cdot 10^{10}$ cm^{-3} at room temperature (from basic semiconductor theory). In the volume shown in Fig. 31 this would correspond to $4.5 \cdot 10^{8}$ free charge carriers; compared to around $3.2 \cdot 10^{4}$ produced by a Minimum Ionizing Particle passing it (corresponding to the Bethe–Bloch energy loss in 300 μm Si divided by 3.6 eV). As result there is a need to decrease number of free carriers. This is done by using the depletion zone between two oppositely doped parts of a silicon wafer.

The zone between the N and P type doping is free of charge carriers, has an electric field and is well suited as detector volume. This zone is increased by applying reverse biasing.

One can quickly establish the most critical parameters for a silicon detector by looking at the p, n junction
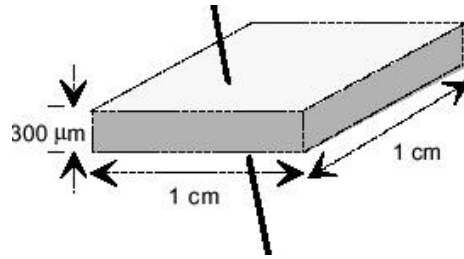
Fig. 31: Sketch of a silicon detector volume

in Fig. 32 above. We use Poisson's equation:

$$\frac{d^2V}{dx^2} = -\frac{\rho(x)}{\varepsilon},$$

with charge density from $-x_p$ to 0 and from 0 to x_n defined by: $\rho(x) = \pm e\, N_{D/A}$. N_D and N_A are the doping concentrations (donor, acceptor): $N_D x_p = N_A x_n$. The depletion zone is defined as: $d = x_p + x_n$.
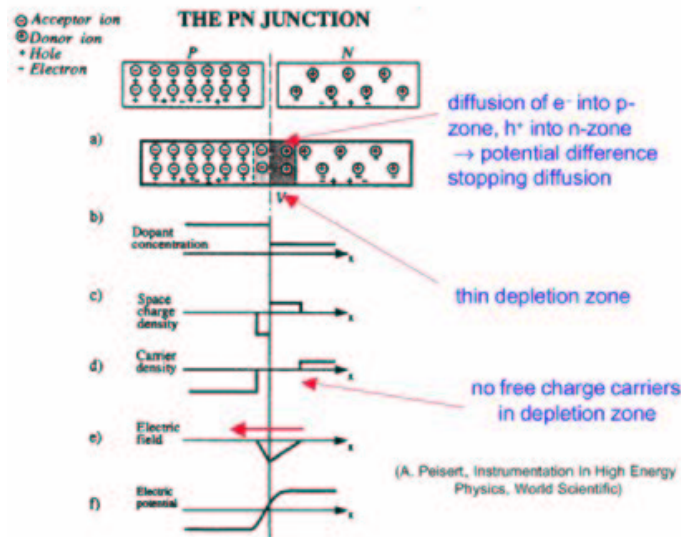

Fig. 32: A silicon pn junction, see references in figure

By integrating one time $E(x)$ can be determined, by integrating twice the following two important relations are found:

$$
\begin{aligned}
V &\propto d^2, \\
C &= \varepsilon\frac{A}{d} \propto V^{-1/2}.
\end{aligned}
$$

By increasing the voltage the depletion zone is expanded and the capacitance C decreased, giving decreased electronics noise.

Let us have look at the signal formation using the same simple model of the detector as two parallel electrodes separated by d. Maintaining a constant voltage across the detector with an external bias circuit,

an electric charge e moving a distance dx will induce a signal dQ on the readout electrode: $dQ\,d = edx$. As in the case of the proportional chamber we use:

$$\frac{dx}{dt} = \mu\,E(x)\,,$$

giving (the charge is created at x_0):

$$x(t) = x_0\,\exp\left(\frac{\mu_e t}{\mu_h \tau}\right)\,,$$

where $\tau = \varepsilon/eN_A\,\mu_h$. The time dependent signal is then:
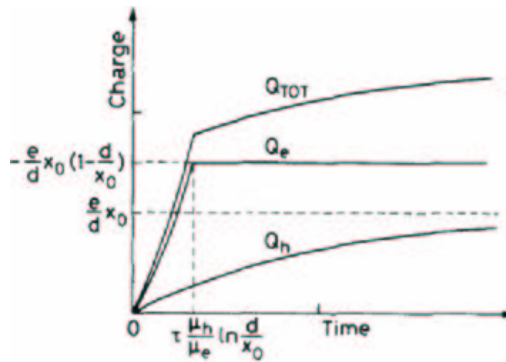
$$Q_e(t) = -\frac{e}{d}\,\int \frac{dx}{dt}\,dt\,.$$

Fig. 33: The final result showing (when entering real numbers and using a more complete model) time-scales of 10/25 ns for electron–hole collection. From Ref. [1].

However, there are many caveats: In reality one has to start from the real $(e - h)$ distribution from a particle. Equally important is to use a real description of $E(x)$ taking into account strips, other implants and over-depletion, only to mention a few key features. Traps and changes in mobility will also enter.

At the moment silicon detectors are used close to the interaction region in most collider experiments and are exposed to severe radiation conditions (damage).
The damage depends on fluence as well as on particle type (proton, γ, e, neutrons, etc) and energy spectrum, and influences both sensors and electronics. The effects are due to both bulk damage (lattice changes) and surface effects (trapped charges).

Three main consequences are seen for silicon detectors (figures from Ref. [2] and Ref. [10]):

[1] Increase of leakage current with consequences for cooling and electronics. This is illustrated in Fig. 36 on the right.
[2] Change in depletion voltage, increasing significantly at the end of the detector lifetime; combined with increased leakage currents this leads to cooling problems again (see Fig. 36).
[3] Decrease of charge collection efficiency.

The future developments for semi-conductor systems address four points in particular (Refs. [10-12]):

[1] Radiation hardness, cost and power consumption. Examples are:
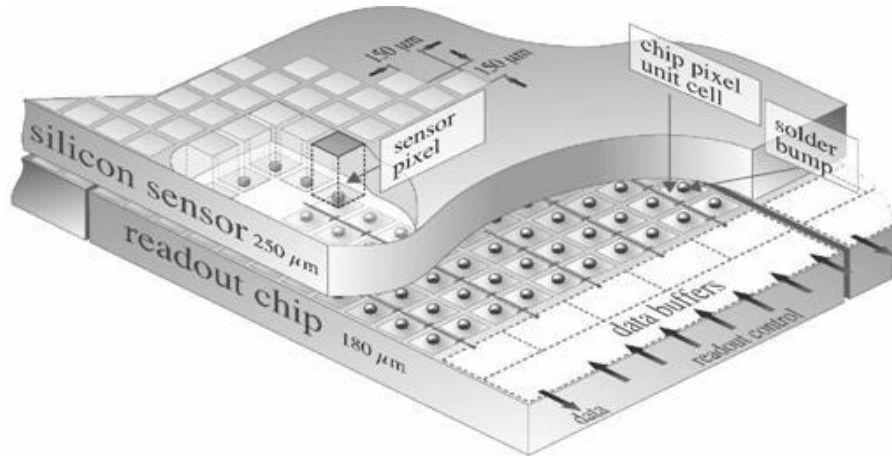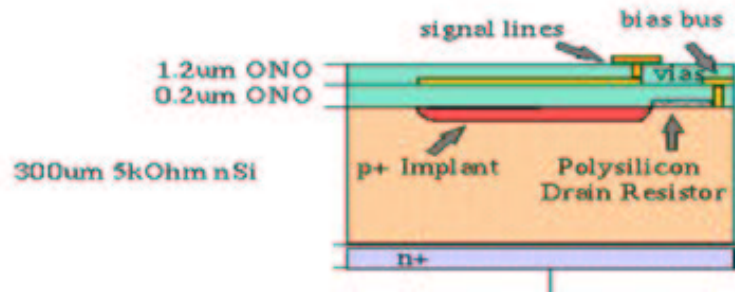   • Defect engineering: Introduce specific impurities in silicon to influence defect formation.

223

Fig. 34: The detectors used in particle physics are usually strip detectors with strip distance 50–100 μm, single or double sided. One example is shown. A more integrated approach is a PIXEL detector also shown below, where the interconnectivity to the readout electronics is made with bump-bonding.

- Cool detectors to cryogenic temperatures.

[2] New materials as for example diamond and amorphous silicon, the latter opens for deposition directly on readout chips.

[3] Integrate the detector and readout on the same wafer.

[4] New detector concept as horizontal biasing for faster charge collection and lower biasing. This will also allow building detectors which are active very close to the physical edge of the wafers.

4.4. Front-end electronics

A concise description of front-end electronics can be found in Ref. [4]. This subsection provides a very short and superficial summary of some of main concepts and constraints.

Most detectors rely critically on low noise electronics and optimal detector performances requires optimized electronics solutions.

The detector is represented by the capacitance C_d, bias voltage is applied through R_b, and the signal is coupled to the amplifier through a capacitance C_c. The resistance R_s represents all the resistances in the input path. The preamplifier provides gain and feeds a shaper which takes care of the frequency response and limits the duration of the signal.

The equivalent circuit for noise analysis includes both current and voltage noise sources labeled in and en respectively. Two important noise sources are the detector leakage current (fluctuating – some times called shot noise) and the electronic noise of the amplifier, both unavoidable and therefore important to control and reduce.
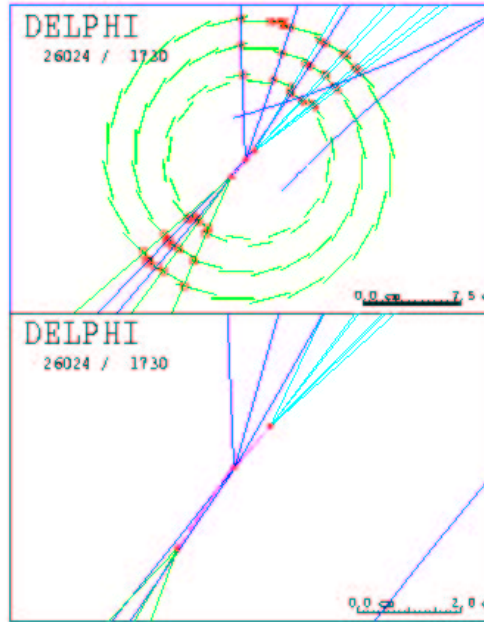
Fig. 35: The microstrip system at LEP were heavily used for B-physics and an example of reconstruction is shown.

While shot noise and thermal noise has a white frequency spectrum (dP_n/df constant), trapping/detrapping in various components will introduce an $1/f$ noise. Since the detectors usually turn the signal into charge one can express the noise as equivalent noise charge, which is equivalent to the detector signal that yields signal-to-noise ratio of one.

Increasing the detector capacitance will increase the voltage noise and shift the noise minimum to longer shaping times. For quick estimates, one can use the following equation (see Ref. [4]):

$$(Q_n/e)^2 = 12 \left[\frac{1}{\mathrm{nA} \cdot \mathrm{ns}}\right] I_d \tau + 6 \times 10^5 \left[\frac{\mathrm{k\Omega}}{\mathrm{ns}}\right] \frac{\tau}{R_b} + 3.6 \times 10^4 \left[\frac{\mathrm{ns}}{(pF)^2 \, (\mathrm{nV})^2/\mathrm{Hz}}\right] e_n^2 \frac{C^2}{\tau},$$

which assumes an FET amplifier with negligible i_{na}, and a simple CR-RC shaper with time constant τ (equal to the peaking time).
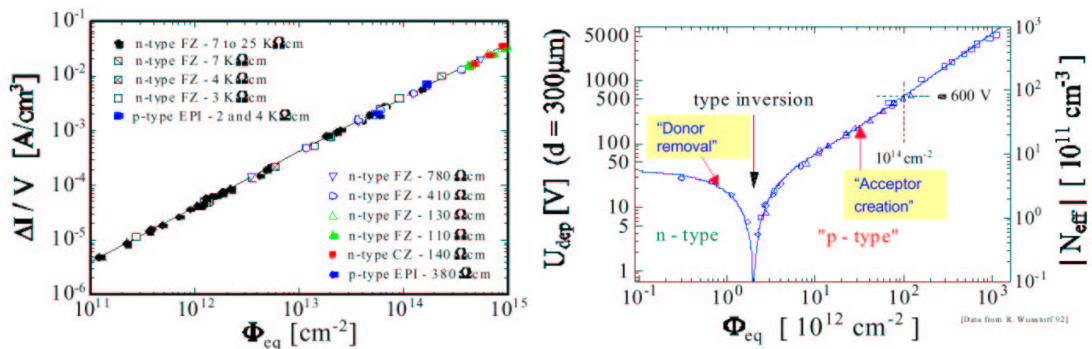

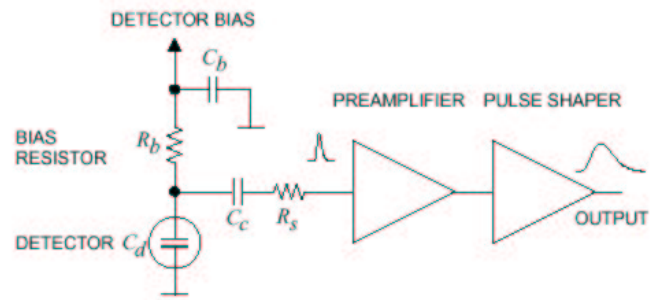Fig. 36: Change of leakage current and biasing voltage as function of fluence.
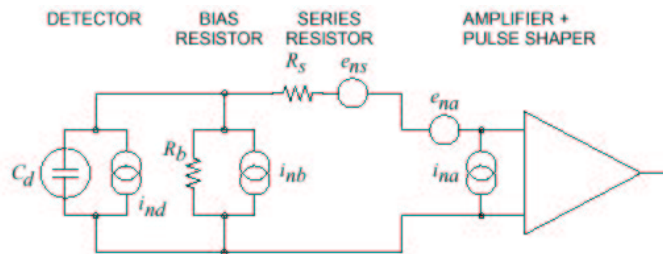
Fig. 37: A typical Front End (Ref. [4]).

Fig. 38: The diagram below show the noise sources and their representation in the noise analysis.
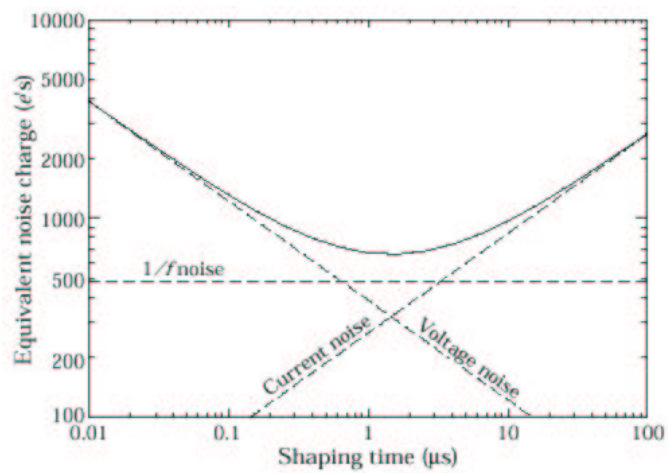

Fig. 39: For the situation we have described there is an optimal shaping time as shown below.

This shows that the critical parameters are detector capacitance, the shaping time τ, the resistances in the input circuit, the leakage current, and the amplifier noise parameters. The latter depends mostly on the input device (transistor) which has to optimized for the load and use. One additional critical parameter, not apparent in the formula above, is the current drawn which makes an important contribution to the power consumption of the electronics.

Practical noise levels vary between 10^2–10^3 ENC for silicon detectors to 10^4 for high capacitance LAr calorimeters (10^4 corresponds to around 1.6 fC).

5. FUTURE

Improved detectors will certainly be needed. Linear colliders, neutrino facilities, astroparticle physics systems, and LHC upgrades will drive the development and things are already happening. Some main areas of research are:

- Radiation hardness will remain a headache. Both for trackers and calorimeters, active detector elements and electronics, and even for support structures and cooling systems.
- Reduce power or deliver power in a more intelligent way (trackers at LHC need of order 100 kW at less than 5 V, current are huge, cables the same to keep losses acceptable). The services complicate the detector integration and compromise the performance.
- Reduce costs for silicon detectors (strip and various pixels). Today a PIXEL detector cost 5–7 MChf per m^2, strip trackers around 0.3–1 MChf per m^2. Similar cost arguments apply to construction of future large muon chamber systems.
- Learn to work at even higher collision frequency (today 40 MHz for LHC).

References

[1] W.R. Leo, *Techniques for Nuclear and Particle Physics Experiments*, Springer-Verlag, ISBN-0-387-57280-5; in particular, see chapters 2,6,7 and 10.

[2] *Particle Detectors*, CERN Summer Student Lectures 2002 C. Joram, CERN. These lectures can be found on the Web via CERN's video pages, and they are also video-taped.

[3] *Instrumentation*, lectures at the 2001 CERN-CLAF School of High-Energy Physics by O. Ullaland, CERN. CERN Report 2003–003.

[4] D.E. Groom *et al.*, Review of Particle Physics; section: Experimental Methods and Colliders; see *http://pdg.web.cern.ch/pdg/*
Chapter 26: Passage of particles through matter.
Chapter 27: Particle Detectors.

[5] B. Dolgosheim, NIM **A326** (1993) 434.

[6] R.L. Gluckstern, NIM **24** (1963) 381.

[7] F. Sauli, Development of high rate MSGCs: overview of results from RD-28. Nucl. Phys. **B61** (1998) 236.

[8] B. Ketzer, Gem detectors for COMPASS, IEEE Trans. Nucl. Sci. NS-48 (2001) 1605.

[9] C. Joram, Nucl. Phys. B (Proc. Suppl.) **78** (1999) 407.

[10] CERN/LHCC 2000-009 LEB Status Report/RD48.

[11] RD39 collaboration status reports. Available via CERN.

[12] Proc. Frontier Detectors for Frontier Physics, 9th Pisa meeting on Advanced Detectors, Elba, 25–31 May 2003.